Journal Pre-proof

Rare earth elemental and Sr isotopic evidence for seawater intrusion event of the Songliao Basin 91 million years ago

Yuke Liu, Huajian Wang, Jinyou Zhang, Zhenwu Liu, Fazi Chen, Xiaomei Wang, Shuichang Zhang, He Liu

PII: S1995-8226(22)00301-6

DOI: https://doi.org/10.1016/j.petsci.2022.11.015

Reference: PETSCI 407

To appear in: *Petroleum Science*

Received Date: 11 April 2022

Revised Date: 23 September 2022

Accepted Date: 18 November 2022

Please cite this article as: Liu, Y., Wang, H., Zhang, J., Liu, Z., Chen, F., Wang, X., Zhang, S., Liu, H., Rare earth elemental and Sr isotopic evidence for seawater intrusion event of the Songliao Basin 91 million years ago, *Petroleum Science* (2022), doi: https://doi.org/10.1016/j.petsci.2022.11.015.

Rare earth elemental and Sr isotopic evidence for seawater intrusion event of the Songliao Basin 91 million years ago

LIU Yuke[1,2], WANG Huajian[1,2,*], ZHANG Jinyou[3,*], LIU Zhenwu[4], CHEN Fazi[4], WANG Xiaomei[1,2], ZHANG Shuichang[1,2], LIU He[1]

[1]*Research Institute of Petroleum Exploration and Development, Beijing 100083, China*
[2] *Key Laboratory of Petroleum Geochemistry, China National Petroleum Corporation, Beijing 100083, China*
[3] *Daqing Oil Field Company, China National Petroleum Corporation, Daqing 163000, China*
[4] *School of Ocean Sciences, China University of Geosciences, Beijing 100083, China*
**Corresponding author: Wang Huajian (wanghuajian@petrochina.com.cn)*
Zhang Jinyou (zhangjinyou@petrochina.com.cn)

Rare earth elemental and Sr isotopic evidence for seawater intrusion event of the Songliao Basin 91 million years ago

Abstract

Petrogenesis of lacustrine dolostone is closely related with paleo-lake water conditions. Here we report the high spatial-resolution petrographic and geochemical results of a lacustrine dolomite nodule from the Qingshankou Formation, the Songliao Basin. Sedimentary and elemental signatures confirm the protogenetic origin of this nodule and its effectiveness in recording geochemical characteristics of paleo-lake water during dolomitization. The low Y/Ho ratios, middle rare earth element (MREE) enrichment and subtle positive Eu anomalies within the nodule indicate a fresh water source. However, the Sr isotope values in the core of the nodule (0.7076–0.7080) are close to contemporaneous seawater (0.7074), yet different from the modern river (0.7120) and the host black shale (0.7100). On the premise of excluding the influence of hydrothermal fluids, the significantly low strontium isotope values of the lacustrine dolomite might be caused by seawater interference during dolomitization. Our findings demonstrate that lacustrine dolomite within black shales is not only a faithful tracer of diagenetic water environment, but also a novel and easily identified mineralogical evidence for episodic seawater intrusion event (91 Ma) in the Songliao Basin, which supplements other paleontological and geochemical evidence.

Keywords: Songliao Basin, lacustrine dolostone, seawater intrusion, rare earth elements, strontium isotope

1. Introduction

Lacustrine dolostones are widely distributed within the Late Phanerozoic to Cenozoic black shales in China, including the Middle Permian Lucaogou Formation in the Junggar and Santanghu basins (Jiao, 2017; Sun et al., 2020), the Late Triassic Yanchang Formation in the Ordos Basin (Zhu et al., 2020), the Late Cretaceous Qingshankou and Nenjiang formations in the Songliao Basin (Liu and Wang, 1997; Gao et al., 2010; Gao et al., 2012), and the Paleogene Shahejie Formation in the Bohai Bay Basin (Yang, 2014). Numerous dolomitization mechanisms have been proposed, including microbial mediation (Xu et al., 2019; Sun et al., 2020), evaporation at early diagenesis (Fruth and Scherreiks, 1982; Zhang et al., 2019), and hydrothermal alternation during shallow burial (Gregg et al., 2015; Yang et al., 2021). Some lacustrine dolostones with centimeter to decimeter sized laminar and nodular features have been supposed to be accompanied with organic matter degradation through biotic (*e.g.*, sulfate reduction, methanogenesis) and abiotic processes (Liu et al., 2020; Sun et al., 2020; Alibrahim et al., 2021). Geochemical information archived in these dolostones are believed to have close relationship with the paleo-lake waters and diagenetic conditions, whereas geological cases and in-depth discussions are still lacking.

The Songliao Basin in northeastern China is a large continental rift basin (Gao et al., 2015), and preserves two organic-rich shales in the Upper Cretaceous Qingshankou and Nenjiang formations (Liu et al., 2019; Zhao et al., 2020; Huang et al., 2021) as a result of lacustrine anoxic events (Wu et al., 2009). However, episodic seawater incursions have also been suggested to favor organic matter preservation with evidence from body fossils (*e.g.*, benthic and planktonic foraminifera, calcareous nano-fossils, marine and brackish-water dinoflagellates, brackish-water fish and bivalves (Xi et al., 2011; Xi et al., 2016), biomarkers (24-*n*-propyl and 24-isopropyl cholestanes) (Bechtel et al., 2012; Hu et al., 2015), and sulfur isotopic compositions of pyrites (Huang et al., 2013; Cao et al., 2016).

Dolostones observed in the Nenjiang black shales in the form of thin layers or nodules were also suggested to have a potential relationship with seawater intrusions (Liu and Wang, 1997; Wang et al., 2008; Gao et al., 2010; Gao et al., 2012).

When reconstructing the sedimentary environment from lacustrine carbonates, rare earth elements plus yttrium (REE+Y) profile has been widely used, due to its high calcite-water partition coefficients (>100) and insensitivity to diagenetic alteration (including dolomitization and meteoric alteration), which outperformed in extracting the linked depositional and diagenetic histories (Wang et al., 2021). Dolomite precipitation from lake water is fundamentally controlled by the thermodynamics, of which the REE+Y patterns can reflect the hydro-geochemical states and the evolutionary processes of terrigenous deep-time freshwater system (Zhao et al., 2021). In this view, REE+Y distribution is commonly considered as a fingerprint for water composition, even for the processes and sources in hydrosphere and lithosphere. Given the fact that REE+Y signatures in carbonates are supremely vulnerable to silicate contamination (Tostevin et al., 2016; Gong et al., 2021), *in-situ* elemental measurement rather than bulk analysis is quite demanding. Recent applications of Laser ablation-inductively coupled plasma-mass spectrometry (LA-ICP-MS) in extracting single-point REE+Y information have been conducted on specific target minerals (O'Connell et al., 2020; Rieger et al., 2021), whereas line-scanning has not been widely utilized. LA based line scanning is outstanding in obtaining subtle geochemical variations with micron spatial resolution. Terrigenous contamination in carbonate rocks could be easily recognized by using this method (Gong et al., 2021). The contamination recognition is of great importance, especially before proceeding isotopic analysis with pure authigenic minerals.

Additionally, strontium (Sr) isotope is an effective indicator to infer the aqueous environment (Bwire Ojiambo et al., 2003; Mearon et al., 2003; Zhou et al., 2020; Ha et al., 2021), for its long residence time (about 10^6 year) in seawater (Stein et al., 2000) and significant fractionation among litho- and hydro-spheres (Faure, 1978; Palmer and Elderfield, 1985), but negligible fractionation during carbonate precipitation and diagenesis (Huang et al., 2011). Marine carbonates with the least alternation are considered to have identical Sr isotopic compositions with contemporaneous seawater (Mountjoy et al., 1992), and the deviation from global Sr isotopic variation curve for lacustrine dolomites can be used to quantify potential seawater addition into paleo-lake (Ha et al., 2021).

Here, we report the high spatial-resolution petrographic, elemental and Sr isotopic compositions of a dolomite nodule from the Qingshankou Formation in the Songliao Basin, by using multiple *in-situ* and micro analytical techniques. Our results provide new evidence that the dolomite nodule might record contemporaneous seawater signals, and thereby can serve as an indicator to trace potential seawater intrusion in the Songliao Basin during Late Cretaceous.

2. Geological setting and sample description

The Songliao Basin in northeast China (**Fig. 1**) underwent three tectonic episodes, rifting, thermal subsidence, and structural inversion (Feng et al., 2010), that preserved approximately 10,000 m of volcaniclastic, alluvial fan, fluvial, and lacustrine sediments (Wang et al., 2013; Wu et al., 2014). Paleomagnetic results reveal a paleolatitude (40–50°N) (Feng et al., 2010) similar to today (42.5–49.5°N). The GY3HC well, located at the deposition center of the Songliao Basin (**Fig. 1a**), contains about 140 m thick strata of Qingshankou Formation, which is mainly composed of the dark mudstones enclosing thin laminae and oval concretions of dolostones. A dolomite nodule encased by black shale (**Fig. 2**) was sampled from Qingshankou Member 1 in GY3HC well. High precision CA-ID-TIMS

zircon U-Pb dating ages (91.886±0.11 Ma, 90.974±0.12 Ma) from the ash layers at the lowermost and uppermost of the first member of Qingshankou Formation, respectively (Wang et al., 2016), constrained the formation time of this nodule to be around 91 Ma.

Fig. 1. (a) Modern schematic map and (b) structural cross section along the central part of the Songliao Basin. Modified from (Huang et al., 2021).

Laminar sedimentary features and the transition from the shale to dolomite nodule can be clearly identified on the sectional surface (**Fig. 2a**). A thin section of area A in **Fig. 2a** covering the nodule and underlying black shale was prepared to do optical observation, mineralogical and *in-situ* elemental analyses (**Fig. 2b**). Seven points avoiding the debris layers in the nodule were selected and sampled by micro-drilling, with points 1-5 from dolomite nodule, point 6 from the transitional area between shale and dolomite, and point 7 from the host shale (**Fig. 2a**). These samples were meshed into powders with a tungsten carbide grinding disc for Sr isotope analysis, and powders from dolostone (point 4) and black shale (point 7) were further investigated for mineralogical and elemental analyses.

Fig. 2. Cross section of dolomite nodule (a), and area A is amplified in (b). Area A in (a) was made for thin section sample and was investigated via *in-situ* XRF multi-element imaging. Power samples were drilled from points 1-7 in (a) to do Sr isotope analysis, and samples form points 4 and 7 were further conducted for ICP-MS analysis. Area B in (b) was observed under optical microscopy. Mineralogical analysis of area C in (b) was conducted via QEMSCAN. Trace elements along line D in (b) was analyzed by LA-ICP-MS.

3. Experimental methods

3.1 Petrographic and mineralogical analyses

The petrographic and mineralogical analyses of dolomite nodule were conducted at Key Laboratory of Petroleum Geochemistry, Research Institute of Petroleum Exploration and Development, Beijing, China. An optical microscope (Olympus 4500P, Olympus Company, Japan) was used to observe the micro-structures of area B in **Fig. 2b** under transmission light. Higher spatial-resolution observation of dolomite was performed on the newly fractured and argon ion polished surfaces by using an Apreo scanning electron microscope (SEM, FEI Company, America) equipped with an integrated high-speed detector (Bruker Company, Germany). Mineral identification of the transitional area between shale and dolostone (area C in **Fig. 2b**) was performed by using a QemScan 650F (FEI Company, America) with a pixel size of 1 μm. Individual minerals were identified by referring to a comprehensive mineral database incorporated into the QemScan software. Powders from point 4 and 7 that represent dolomite and shale, respectively, were pressed into 1-cm-diameter cakes to determine the mineralogical compositions by using an X-ray diffraction (XRD, Rigaku SmartLab Company, Japan) equipped with a Cu tube and a monochromator. The working voltage and current of the X-ray generator were 40 kV and 150 mA, respectively. Scan range (2θ) was selected from 2.6° to 45° with an interval of 0.02°.

3.2 Elemental geochemical analysis

Multi-element imaging was performed on a M4 Tornado X-ray Fluorescence (XRF, Bruker Company, Germany) at Key Laboratory of Petroleum Geochemistry, Research Institute of Petroleum Exploration

and Development, Beijing, China. The whole thin section shown in **Fig. 2b** were full-coverage scanned with a 20-μm-diameter X-ray beam and a single-point exposure time of 200 ms. The X-Ray was derived from a Rh anode with a working voltage of 50 kV and a working current of 200 μA at 20 Mbar atmospheric pressure. In vacuum state, the energy spectrum emitted by the Rh tube is primarily suitable for the elemental measurements from Na to U. Here, the information of Ca, Mg, Fe, Mn, Sr, Si, Al, S that related to the dolomite, quartz, pyrite and clay minerals were extracted and imaged with a spatial resolution of 25 μm.

Trace element contents of the powders sampled from the points 4 (dolomite) and 7 (shale) in **Fig. 2a** were determined by using an ELEMENT XR ICP-MS (Thermo Fisher Company, America) at Key Laboratory of Petroleum Geochemistry, Research Institute of Petroleum Exploration and Development, Beijing, China. For each sample, approximately 50 mg powders were weighted and placed in a Teflon bomb. The powders were dissolved in the mixed solution of 1 ml HNO_3 and 1 ml HF under 10 MPa and 180 ^{o}C conditions. The digestion time was about 8 h to achieve complete dissolution of rocks. Uncertainty estimates of each measured element is based on the synchronous digested reference material of MACS-3. The relative standard deviation (RSD) of each measured element is lower than 3%.

In-situ element analysis was performed on a RESOlution 193 nm LA (Australian Scientific Instruments, Australia) coupled with a PlasmaQuant MS Elite ICP-MS (Analytik Jena AG Company, Germany) at Beijing Createch Testing Technology Co., Ltd., Beijing, China. Line D in **Fig 2b** was selected for laser ablation with a spot size of 50 μm and a scanning rate of 50 μm/s. Helium (He) was used as a carrier gas to transport aerosol from sample surface to ICP-MS, and Argon (Ar) was used as a make-up gas. Operational parameters of the LA and ICP-MS were tuned for maximum sensitivity, low oxide formation based on the $^{232}Th^{16}O/^{232}Th$ ratio and low laser-induced elemental fractionation based on the $^{232}U/^{232}Th$ ratio by using certified reference material NIST 610. The laser repetition rate was 10 Hz with an energy density of 6 J/cm^2. The dwell time of each element of ICP-MS was 10 ms. Data was analyzed by using the software of Iolite 3.25 (Paton et al., 2011). Uncertainty estimates of each measured element are based on repeated measurement of MACS-3. Under the optimized conditions, the RSD of each measured element is lower than 10%.

3.3 Strontium isotope analysis

Powder samples from points 1-7 in **Fig. 2a** were selected for Sr isotope analysis at Beijing Research Institute of Uranium Geology, China National Nuclear Corporation, Beijing, China. About 50–70 mg of the sample was dissolved in 2.5 N HCl for 1–2 h at room temperature. The solutions were centrifuged, and the supernatant was recovered. Soluble Sr was further separated by using an ion-exchange column packed with Bio-Rad AG 50W-X12 resin. Sr isotope analyses were measured on a Finnigan MAT-262 multi-collector thermal-ionization mass spectrometer (TIMS, Finnigan Company, Germany). The standard reference sample NBS-987 was used for quality control and the measured value of the $^{87}Sr/^{86}Sr$ ratio was 0.710240 ± 0.000005 (n=10).

3. Results

3.1 Mineralogical and petrographic compositions

The dolomite nodule is mainly composed of dolomite (70.2 %) with small amounts of quartz (14.0 %) and clay minerals (15.8 %) (**Fig. S1a**). As a contrast, the host black shale mainly contains clay minerals (54.0 %) and quartz (29.1 %), with small proportion of feldspar (12.1 %) and dolomite (4.8 %) (**Fig. S1b**). Distinct sedimentary characteristics with debris layers in the nodule (**Fig. 3a**) indicate its authigenic genesis. Angular quartz and feldspar grains preserved in the debris layers (**Fig. 3b**), are typical protogenetic characteristics representing terrestrial silicate contamination. Apart from debris

layers, the nodule has micro-lithic structures composed of fine-grained euhedral-subhedral dolomite crystals (**Fig. 3c**). Presence of ankerite was confirmed by the blue-colored grains after dyed with alizarin red (**Fig. 3c**). The transitional zone from underlying black shale to dolomite nodule contains several terrestrial debris layers (**Fig. 3a**), enclosing sub-rounded to angular quartz grains and dark-colored iron-rich minerals (**Fig. 3d**).

Fig. 3. Photomicrographs of the transient zone from black shale to dolomite nodule of area A in **Fig. 2a**, under microscopic transmission light. Laminar terrigenous debris in the nodule are pointed out by yellow arrows. Quartz particles with poor roundness (b), dolomite grains with micro-lithic structure (c) and silty layer (d) are shown in the right-hand enlarged views.

Mineralogical distribution obtained from QemScan further distinguished the dolostone nodule into 4 zones: black shale with clay minerals (*e.g.*, illite, chlorite) and quartz (zone a in **Fig. 4**), silty layer composed of quartz and albite (zone b in **Fig. 4**), transitional area with quartz, albite, and chlorite (zone c in **Fig. 4**), and the dolostone nodule with dolomite grains (zone d in **Fig. 4**). A thin terrigenous lamina with quartz and albite was recognized at the beginning of dolomite precipitation (pointed with white arrow in zone d in **Fig. 4**). It is interesting to note that pyrite crystals are easily recognized within the transitional area and dolomite nodule (pointed with yellow arrows in zones c and d in **Fig. 4**), but not in the silty layer and black shale (zones a and b in **Fig. 4**). Under SEM, the dolomite grains show rhombohedron of euhedral-subhedral shape with diameters of micro- to centimeters (**Figs. 5a and b**). The dark nucleus and light rim within a single dolomite crystal are demonstrated to be dolomite and ankerite, respectively (**Figs. 5c and d**). Organic matter is occasionally observed while being accompanied with ankerite, chlorite (**Figs. 5c and d**), and pyritohedron-type pyrite crystals (diameters of 1–4 μm) (**Fig. 5d**).

Fig. 4. Scanning electron microscopic image and mineralogical distribution of area C in **Fig. 2b** via QEMSCAN (spatial resolution=1.5 μm). Four sections are recognized, including zone a: host black shale, zone b: silty layer, zone c: shale with numerous siliceous detritus embedded, and zone d: dolomite nodule. Detritus lamina and pyrite are marked by white and yellow arrows, respectively.

Fig. 5. Scanning electron microscope photos of newly fractured (a and b) and argon ion polished facies (c and d) of dolomite. The dolomite crystals aggregate in a cumulative texture (a) with rhombus euhedral-subhedral shapes (b). Organic matter residues (c and d) are accompanied by pyrite occasionally (d).

3.2 Elemental contents and distributions

The elemental images based on μ-XRF of the thin section sample (**Fig. 6a**) are shown in **Figs. 6b-i.** Quantitative elemental variations via LA-ICP-MS along the green dashed line in **Fig. 6a** are correspondingly plotted at the right sides in **Figs. 6b-i**. Contents of selected trace elements (Th, Zr, V, Ni, Co) and sum of REE+Y (∑REE+Y) from LA-ICP-MS and solution-based ICP-MS are shown in **Fig. 6j**. Good consistencies on the results from μ-XRF, LA-ICP-MS and ICP-MS (**Fig. 6, Tables 1-2**), indicate that the elemental record could provide detailed information of diagenetic water environment. Compared with the host black shale, the dolomite nodule is supremely concentrated with Ca, Mg, Fe,

Mn and Sr, whereas depleted in redox sensitive elements (*e.g.*, V, Ni, Co), terrestrial elements (*e.g.*, Si, Al, S, Th, Zr), and REE+Y. Notably, Ca, Mg, Fe, Mn and Sr are not homogenously distributed within the nodule but exhibiting layered patterns. Ca, Mg and Sr are specifically enriched in the core with quantitative contents of 22%, 10% and 0.2 %, respectively, while decrease slightly to 19%, 8.5% and 0.15% in the rim. Comparatively, Fe is more abundant in the rim (9.5%), with a slightly lower content (7%) in the core. Mn is intensively enriched in the transitional area, with a maximum content of 0.7%, but vanishes rapidly towards dolomite (0.24%) and shale (0.04%). The silty layer is depleted in S but enriched in Fe (6%) compared with surrounding black shale (Fe=3.5%).

Fig. 6. (a) $^{87}Sr/^{86}Sr$ values from different micro-areas of the dolomite nodule (area A in **Fig 2a**). Corresponding images of Ca (b), Mg (c), Fe (d), Mn (e), Sr (f), Si(g), Al(h), S(i) obtained from XRF scanning with 20-μm pixel size and 4-ms exposure time per pixel. The imaging size was 54.9 × 46.4 mm with 2745 × 2320 pixels. The right-hand data of (b-i) and (j) were obtained from LA-ICP-MS scanning along the green dash line in (a). Elemental contents obtained from solution ICP-MS are marked with red dash lines in (j). REE patterns of dolomite (arrow A in c), Fe-rich dolomites (arrows B and C in d) and S-rich lamina (arrow D in i) are shown in **Fig. 8b.**

Table 1. Averaged REE+Y contents (ppm) of different sections in nodule based on LA-ICP-MS and ICP-MS methods.

Sample	Method	La	Ce	Pr	Nd	Sm	Eu	Gd	Tb	Dy	Y	Ho	Er	Tm	Yb	Lu	∑REE+Y
Shale 1	LA-ICP-MS	36.87	45.71	6.88	20.50	4.08	0.68	2.90	0.46	2.89	16.55	0.60	1.68	0.26	1.78	0.27	142.10
Detritus		18.15	43.82	5.77	25.43	5.60	1.08	4.13	0.50	2.53	12.91	0.42	0.97	0.15	0.92	0.13	122.50
Shale 2		25.60	50.47	7.19	21.49	4.54	0.97	3.83	0.61	3.54	17.66	0.62	1.73	0.25	1.68	0.25	140.41
Transition		18.79	42.82	4.78	19.92	4.56	1.02	4.09	0.67	3.74	20.62	0.72	1.80	0.26	1.70	0.26	125.76
Fe-dolomite		8.72	18.51	2.10	9.44	2.37	0.57	2.27	0.35	1.89	11.12	0.35	0.87	0.13	0.84	0.13	59.66
Mg-dolomite		8.34	17.92	2.11	9.52	2.23	0.57	2.14	0.33	1.79	10.82	0.32	0.81	0.11	0.77	0.12	57.92
Shale	ICP-MS	37.90	69.40	8.02	30.30	4.75	0.89	4.39	0.73	4.22	21.90	0.79	2.37	0.37	2.42	0.37	188.82
Dolomite		7.16	16.10	2.05	9.34	2.04	0.45	1.72	0.34	1.92	9.93	0.35	0.92	0.14	0.88	0.14	53.48

Table 2. Trace elemental contents (ppm) of shale and dolomite based on ICP-MS method.

	Th	Zr	V	Ni	Co
Shale	11.5	155.0	124.0	13.0	20.5
Dolomite	1.2	16.8	40.9	2.0	16.0

The raw REE+Y contents via ICP-MS and LA-ICP-MS were normalized to Post-Archaean Australian Shale (PAAS) (McLennan, 1989). Anomalies of Ce and Eu and the partitioning of middle REEs (BSI) were calculated as (Lawrence et al., 2006):

$$\left(Ce/Ce^{*}\right)_{SN} = Ce_{SN} \Big/ \left(Pr_{SN} \times \left(Pr_{SN}/Nd_{SN}\right)\right) \quad (1)$$

$$\left(Eu/Eu^{*}\right)_{SN} = Eu_{SN} \Big/ \left(Sm_{SN}^{\ 2} \times Tb_{SN}\right)^{1/3} \quad (2)$$

$$BSI = \frac{2\times\left(Sm_{SN} + Gd_{SN} + Dy_{SN}\right)}{3} \Big/ \left(\frac{La_{SN} + Pr_{SN} + Nd_{SN}}{3} + \frac{Ho_{SN} + Er_{SN} + Tm_{SN} + Yb_{SN} + Lu_{SN}}{5}\right) \quad (3)$$

It is worthy of mentioning that Eu abundance may be originated from test error due to the interference of Ba element. Since $^{151}Eu^{+}$ and $^{135}Ba^{16}O^{+}$ share the similar valence state and ion radius, the existence of Ba oxide and hydroxide in geological samples with high Ba content could seriously affect the accurate measurement of Eu (Planavsky et al., 2010). Here, the analytical artefact on positive Eu anomaly could be ruled out for the absence of any correlation between laser-ablation based Ba and $(Eu/Eu^*)_{SN}$ (**Fig. S2**).

After a 35-points moving-average on raw dataset to eliminate signal oscillations, the REE+Y patterns of dolomite nodule and host black shale, including ∑REE+Y, BSI, Y/Ho, $(Ce/Ce^*)_{SN}$ and $(Eu/Eu^*)_{SN}$ are illustrated in **Fig. 7**. The measured ∑REE+Y shows a gradual decline from shale (142 ppm) to transitional area (120 ppm) and dolomite nodule (55 ppm). In general, both BSI and Y/Ho values show rising trends with fluctuations from shale to dolostone, with particularly high values in silty layer. The BSI value is relatively low in shale (from 1.0 to 1.4), but bumps in silty layer (1.7) and increases within dolomite nodule from rim (1.5) to core (1.9). Similarly, the Y/Ho ratios are 30 in shale and 43 in silty layer, and increase from the rim (32) to core area (46) in dolomite nodule. Both $(Ce/Ce^*)_{SN}$ and $(Eu/Eu^*)_{SN}$ show positive anomalies and oscillate between 1.0 and 1.5. A sustained increasing trend of $(Eu/Eu^*)_{SN}$ could also be recognized from shale to dolomite nodule, which was confirmed by the statistical results from LA-ICP-MS (**Fig. S3**).

Fig. 7. ΣREE+Y contents, BSI, Y/Ho ratios, $(Ce/Ce^*)_{SN}$ and $(Eu/Eu^*)_{SN}$ data of the LA-ICP-MS scanning line in **Fig. 6a**. The data shown here are the results of 35-point moving average of the raw data obtained from LA-ICP-MS.

As revealed from bulk analysis via ICP-MS (**Fig. 8a, Table 1**), REE+Y pattern of black shale is rather flat, different from the specific "dome" structure of dolomite nodule. Shale has high ∑REE+Y (188.8 ppm) and low Y/Ho ratio (27.72), while dolomite has low ∑REE+Y (53.48 ppm) but high Y/Ho ratio (28.37). To get the detailed view of varied REE+Y patterns along the nodule profile, averaged LA-ICP-MS based REE+Y patterns of different phases, i.e., shale 1, silty layer, shale 2, transitional zone, Fe-rich dolomite and Mg-rich dolomite classified in **Fig. 6a** are illustrated in **Fig. 8a**. Black shale (shale 1) has higher ∑REE+Y (142.1 ppm), a rather flat REE+Y pattern and low Y/Ho ratio (27.43). Shale 2 has similar REE+Y profile with a ∑REE+Y of 140.61 ppm, a Y/Ho ratio of 28.66, and a BSI value of 1.20. The silty layer between shale 1 and 2 is MREE-enriched with a BSI value of 1.68, a decreased ∑REE+Y of 122.5 ppm and an increased Y/Ho ratio of 30.57. Transitional zone towards dolomite exhibits a slight enrichment of MREE (BSI=1.40), a ∑REE+Y of 125.76 ppm and a Y/Ho ratio of 28.81. To specifically identify the terrigenous contamination in dolostone, a particular REE+Y pattern of sulfur-rich lamina within dolostone (D in **Figs. 6 and 8b**) was selected and compared with pure dolomite (A-C in **Figs. 6 and 8b**). Noticeable MREE-enriched pattern (BSI=2.70) and super-high ∑REE+Y (1161.3 ppm) of the S-rich lamina confirm the interference of terrigenous contamination. However, no obvious differences are found in REE+Y patterns between Mg- and Fe-dolomites, with BSI values varying from 1.45 to 1.66 and ∑REE+Y from 54.5 to 66.0 ppm.

Fig. 8. Averaged PAAS-normalized REE+Y patterns of (a) different segments in **Fig. 6a,** and (b) areas A-D in **Fig. 6**. Results from ICP-MS are shown for comparison. Parameter of "n" is the total

points number for averaging.

3.3 Strontium isotope composition

Sr isotope composition exhibits a decreasing trend from shale (0.709972) to transitional area (0.707987) and remains steady within dolomite nodule (from 0.7076004 to 0.707646) (**Fig. 6a, Table 3**).

Table 3. Strontium isotope compositions of the samples from points 1-7 in **Fig. 2a.**

Point	Lithofacies	$^{87}Sr/^{86}Sr$	Std.
1	Dolomite	0.707646	0.000014
2	Dolomite	0.707626	0.000016
3	Dolomite	0.707605	0.000019
4	Dolomite	0.707602	0.000013
5	Dolomite	0.707600	0.000014
6	Transition	0.707987	0.000018
7	Shale	0.709972	0.000013

4. Discussion

4.1 Terrigenous contamination in dolomite nodule

Terrigenous detritus could be captured by carbonates at early diagenesis (Azmy et al., 2011). Since trace elements in terrigenous detritus are higher than pure carbonates, a small proportion of detritus contamination could significantly elevate the trace element contents in bulk carbonate rocks. Similarity of REE+Y patterns between silty layer and dolostone indicates a potential terrigenous contamination in dolomite nodule, which is confirmed by the laminar clastic layers within dolomite nodule (**Figs. 2 and 3**). In this view, it is important to rule out the contaminants before using the REE+Y profiles of dolomite nodule to infer their diagenetic water environment.

Due to extremely low solubility and short residence time in water, the element of Th is supremely enriched in terrigenous detritus when compared with pure carbonates (Taylor and McLennan, 1985), and is widely used as a tracer of terrigenous contamination for carbonates (Zhao and Zheng, 2014; Gong et al., 2021). As shown in **Fig. 9a**, great consistency has been confirmed between Th and ∑REE+Y. REE+Y patterns via LA-ICP-MS for silty layer, Fe-dolomite and Mg-dolomite phases were classified into several groups according to Th contents (**Figs. 9b-d**). For both Fe- and Mg-dolomites, samples with low Th contents (<2 ppm) display similar bump-shaped REE+Y features with the averaged results (**Figs. 9c-d**). Then a 2-ppm-Th content in lacustrine dolostone was set as distinguishing criteria, above which terrigenous contamination could not be ignored. This threshold is a little higher than the criteria for marine carbonates at 0.5 ppm (Gong et al., 2021) or 1.0 ppm (Zhao and Zheng, 2016). Such discrepancy might be attributed to the abundant terrigenous clastic materials deposited in paleo-lakes when compared with ocean. The content of Th for dolomite nodule is as low as 1.2 ppm (**Table 2**), being far less than the host black shale (11.5 ppm). Furthermore, most LA-based data possess a Th content lower than 2 ppm (**Fig. 6i**). Combined with the elemental distribution given by μ-XRF, anomalous high REE+Y values are attributed to S-rich debris laminae (**Fig. 8b**). After eliminating the terrigenous contamination, the REE+Y patterns are qualified to reflect the diagenetic water environment during dolomitization (Ye et al., 2020; Gong et al., 2021).

Fig. 9. (a) Relationship between Th and ΣREE+Y contents for different petrographic phases based on LA-ICP-MS data (R^2 is linear correlation coefficient) (a). PAAS-normalized REE+Y patterns of silty layer (b), Fe-dolomite (c) and Mg-dolomite (d) with different Th contents. The "Averaged" REE+Y patterns in light grey (b-d) are the mean values of all laser points data.

4.2 Lacustrine geochemical characteristics recorded in dolomite nodule

The features of REE+Y patterns in carbonates are thought to be insensitive to diagenetic alteration, in spite of multiple post-depositional dolomitization events (Nothdurft et al., 2004). Different from relatively homogeneous seawater, the more variable REE+Y patterns in lake water are supposed to reflect multiple contributions of continental weathering and preferential removal of REE+Y from solutions by colloids or authigenic minerals (Johannesson et al., 1996; Sasmaz et al., 2021). Reactions between dissolved and non-dissolved materials play a dominant role in determining REE+Y compositions in lake water (Johannesson et al., 1996). The authigenic lacustrine dolomite nodule here is suggest to keep its pristine chemistry inherited from lake water, which is featured with MREE enrichment, relatively low Y/Ho, slight positive Eu and Ce anomalies in general.

4.2.1 MREE enrichment

Similar MREE-enriched patterns observed here had been reported for other carbonates (Bolhar and Kranendonk, 2007; Skinner et al., 2019) (**Fig. S4**). Hydrothermal fluid is a possible source of MREE-enriched lacustrine dolomites (Bolhar and Kranendonk, 2007; Yang, 2014). However, the reported Cretaceous hydrothermal lacustrine dolomite was enriched with heavy REE (HREE) (Li et al., 2020; Yang et al., 2020), and these hydrothermal related lacustrine dolomites can be distinguished from specific high-temperature related minerals (*e.g.*, natrolite and analcime) or hydrothermal metasomatic origin (Rieger et al., 2021), whereas none of these has been observed in dolomite nodule here. Bump-shaped REE+Y patterns have been widely recognized in various terrestrial waters, including rivers (Lawrence et al., 2006; Kim et al., 2020), acid lakes (Johannesson et al., 1996; Bwire Ojiambo et al., 2003), groundwater (Pourret et al., 2010) and hydrothermal-influenced lakes (Sasmaz et al., 2021). MREE-enriched pattern in lacustrine carbonates is supposed to be mainly documented in low-pH waters, but not high-pH systems (i.e., modern seawater) or alkaline lakes (Johannesson et al., 1996). Processes leading to such REE+Y profiles include colloidal association, particle/mineral-liquid interaction, phosphate complexation and sulfate complexation (Bolhar and Kranendonk, 2007), whereas the most dominant contributor may be Fe-Mn-rich particulates and their surface coatings within aquifer materials (Haley et al., 2004). The possibilities of phosphate minerals and organic flakes as alternative REE+Y hosts could be ruled out here for their relatively low contents. In the process of dissimilatory iron reduction, the mole ratio of organic carbon and Fe oxides is 1:4, indicating more Fe-oxides were reduced while releasing REE+Y into the water when compared with organic matters. Given the enriched Fe and Mn elements in dolomite (**Figs. 6d and e**), MREEs are supposed to be mainly released from Fe-oxyhydroxides during iron reduction under sub-oxic porewater condition and subsequently trapped in the carbonates.

4.2.2 Y/Ho ratio

Although Y and Ho exhibit similar geochemical behaviors, Ho is preferentially complexed and removed from fluids by Fe-oxides and organic particles (Dulski, 1997). Consequently, seawater preserves super-chondritic Y/Ho values (>28), whereas crustal fluids have chondritic ones (<28) (Smrzka et al., 2019). It has been suggested that modern seawater displays substantially higher Y/Ho ratio (60–90) than terrestrial water (26) (Lawrence et al., 2006). Studies on the South East Queensland Waterways

suggested that water with high salinity (3.7%–4.1%) typically have the highest Y/Ho ratios (32–39) (Lawrence et al., 2006), and the Y overabundance is likely due to addition of seawater with a Y/Ho ratio of 55 (Snidvongs, 2000). For our dolomite nodule concerned here, increased Y/Ho values from 27.46 in shale to 33.34 in the core of nodule (**Table 1, Fig. 7**), indicate a freshwater-dominated source and an interference of seawater to depositional environment. Notably, although more Ho would be released during the reduction of Fe-Mn oxides, while leading to a decreased Y/Ho of anoxic manganous/ferruginous water (Dulski, 1997), the dolomite here still shows a positive Y anomaly, which indicates an even higher Y/Ho value of bottom lake water during dolomite formation.

4.2.3 Positive Ce and Eu anomalies

Throughout the whole nodule section, the positive Ce anomaly is rather subtle in dolomite (**Fig. 7**). The weak positive Ce anomalies in carbonates is a result of excessive Ce captured from water column, which was released from Fe-Mn oxides dissolution under suboxic water conditions (Bau and Möller, 1992). Apart from oxygen fugacity, relative Ce abundances in fresh water are found to depend on pH (Pourret et al., 2010), dissolved organic carbon concentration (Dia et al., 2000), Fe and Mn oxidative scavenging and surface complexation (Carlo et al., 1997), and the mobility during continent-sourced weathering (Patino et al., 2003), among which pH plays the most dominating role. Intensive negative Ce anomalies usually occur at high pH condition, but disappear at low pH condition (Bau and Möller, 1992; Lawrence et al., 2006). Combined with the MREE-enrichment feature, the weak positive Ce anomaly here may be contributed to suboxic near-surface porewater condition.

Eu anomaly displays an increasingly positive inclination with sedimentation, especially in the core of dolomite nodule (**Fig. 7**). After excluding the contribution of hydrothermal fluids as the most common factor related with positive Eu anomaly (Hecht et al., 1999; Jiang et al., 2021; Rieger et al., 2021; Yang et al., 2021), substitution of Ca^{2+} and entering the carbonate lattice in reduced environment is another possible reason (Bau and Möller, 1992). In terrestrial waters, pronounced Eu enrichment in dissolved loads may be ascribed to enhanced dissolution from suspended particles and higher stability in salty solution (Goldstein and Jacobsen, 1988). Lake environment was indeed a complex system, where local aquifer commonly interacts with freshwater, hydrothermal fluids and intruded seawater (Bwire Ojiambo et al., 2003). In this view, the slight positive Eu anomalies here may be attributed to elevated salinity level due to seawater intrusions and substitution of Ca^{2+}.

4.3 Seawater geochemical characteristics archived in dolomite nodule

Before extracting geochemical signals from the lacustrine dolomite, mineral contamination (*e.g.*, terrestrial detritus, Fe-Mn oxides, and sulfides) needs to be critically assessed by plotting correlation diagrams between Y/Ho ratios and representative trace elements (*e.g.*, Th, Ni, Sc) that are preferably incorporated into these interfering mineral phases (Zhao, 2016). The Y/Ho ratios of dolomite show no dependency on Th, Ni and Sc (**Fig. 10**), further indicating the negligible contaminations.

Fig. 10. Relationships between Y/Ho and (a) Th, (b) Ni and (c) Sc for different petrographic phases.

4.3.1 Evidence from REE+Y

REE+Y inventories archived in lacustrine dolomite could be used to distinguish possible marine contribution from lacustrine system (Bolhar and Kranendonk, 2007; Ha et al., 2021). Different from terrigenous fresh water with flat REE+Y profile and low Y/Ho ratio, seawater normally exhibits light REE (LREE)-depleted REE+Y profile and high Y/Ho ratio (>45), which appear remarkably coherent throughout time as fingerprints of seawater (Bolhar and Kranendonk, 2007; Lawrence et al., 2006;

Sasmaz et al., 2021). Values of $(Nd/Yb)_{SN}$, $(Nd/Er)_{SN}$ and $(Sm/Er)_{SN}$ represent the ratios of LREE/HREE, LREE/MREE, and MREE/HREE, respectively, which corporately define the REE+Y pattern. The Y/Ho ratio is believed to be positively related with seawater contribution (Bolhar and Kranendonk, 2007; Ha et al., 2021). Then, the relationships of Y/Ho with $(Nd/Yb)_{SN}$, $(Nd/Er)_{SN}$ and $(Sm/Er)_{SN}$ of carbonates could be used to quantify the mixing of marine and terrestrial waters (Zhao and Zheng, 2016). With the assumption that seawater-sourced REE patterns have remained almost unchanged throughout the Phanerozoic Era (Shields and Webb, 2004), Carboniferous-Permian seawater and freshwater (Zhao, 2016) are referred here as two end members. As shown in **Fig. 11**, this dolomite displays predominant fresh-water-sourced REE+Y signals with slight seawater interference.

Fig. 11. Relationships between Y/Ho and (a) $(Nd/Yb)_{SN}$, (b) $(Nd/Er)_{SN}$, (c) $(Sm/Er)_{SN}$ based on LA-ICP-MS results for dolostone nodule. Data obtained from solution ICP-MS are marked with yellow triangles. Cretaceous-Permian seawater (purple diamond) and freshwater (blue diamond) are two end members (Zhao, 2016). Mixtures with 1%, 5% and 20% proportions of fresh water are labeled with white cycles.

4.3.2 Evidence from strontium isotope

$^{87}Sr/^{86}Sr$, as one of the most stable isotopes on earth, has been widely used as an effective indicator to infer the nature of dolomitizing fluids or even constrain the time of formation. Throughout the geological time, Sr isotope has been severely fractionized between crust (0.7205) (Faure, 1978) and mantle fluid (0.7035) (Palmer and Elderfield, 1985). Since the residence time of strontium in seawater (10^6 year) is several orders of magnitude greater than the mixing time (10^3 year) of seawater, it is hypothesized that ocean has a homogeneous Sr isotopic value throughout the geologic time, from which a strontium isotope stratigraphy can be built (Stein et al., 2000; Bosio et al., 2020; Zhou et al., 2020). The radiogenic Sr isotope compositions of seawater and marine carbonates are rather homogeneous (Fantle et al., 2020). As diagenetic alteration and dissolution of bulk carbonates merely make their $^{87}Sr/^{86}Sr$ values 0.0001–0.0002 lower than that of seawater (Chanda and Fantle, 2017), the $^{87}Sr/^{86}Sr$ values of carbonates are mainly dominated by input fluxes of radiogenic Sr (McArthur et al., 2012). Due to the influences of terrestrial and mantle-sourced hydrothermal inputs, Sr isotopic composition of seawater varies dramatically throughout the geological time, but still lies between the compositions of river water (0.7120) (Palmer and Edmond, 1989) and the mantle-sourced hydrothermal fluid (0.7035).

A mixing of terrestrial Sr during lacustrine carbonate sedimentation might severely increase Sr isotope from the original lake water value (Jacobsen and Kaufman, 1999). The $^{87}Sr/^{86}Sr$ values of lacustrine carbonates are typically higher than the contemporaneous seawater due to riverine input from the continents, including the Late Triassic Yanchang Formation in the Ordos Basin (0.711222–0.711594) (Zhu et al., 2020), the Early Cretaceous Xiagou Formation in the Jiuquan Basin (0.71225–0.71781) (Wen et al., 2009), the Paleogene Shahejie Formation in the Bohai Bay Basin (0.7086–0.7108) (Yang, 2014) and the Late Cretaceous Nenjiang Formation in the Songliao Basin (0.70780±0.0005) (Liu and Wang, 1997) (**Fig. 12**). However, the $^{87}Sr/^{86}Sr$ values of some lacustrine carbonates would be severely decreased (lower than the seawater) due to contribution of mantle-sourced hydrothermal fluid, such as the Middle Permian Lucaogou Formation in the Santanghu Basin (0.704618–0.705254) (Jiao, 2017) and Junggar Basin (0.705687) (Zhang et al., 2020) (**Fig. 12**).

Fig. 12. Strontium isotopic data of dolomite nodule in this study (cycles) and previously reported lacustrine dolomites (squares), seawater (blue line; Mearon et al., 2003), crust (orange line; Faure, 1978)

and mantle (red line; Palmer and Elderfield, 1985). Permian dolomites in the Junggar Basin and Santanghu Basin are referred from Jiao (2017) and Zhang et al. (2020), respectively. Triassic dolomite in the Ordos Basin is referred from Zhu et al. (2020). Cretaceous dolomite in the Jiuquan Basin is referred from Wen et al. (2009). Cretaceous dolomite in the Songliao Basin is referred from Liu and Wang (1997). Paleogene dolomite in the Bohai Bay Basin is referred from Yang (2014).

The $^{87}Sr/^{86}Sr$ values within the dolomite nodule (points 1-6) remained at 0.7076005–0.7079870, being close to the contemporaneous seawater (0.7074) (Bwire Ojiambo et al., 2003), whereas far less than the underlying black shale (point 7 with $^{87}Sr/^{86}Sr$=0.709972). Compared with other Cenozoic-Mesozoic lacustrine dolomites formed in fresh lake water with low salinity ($^{87}Sr/^{86}Sr>0.710$), the relatively low $^{87}Sr/^{86}Sr$ value here may be attributed to the contribution of seawater. Sr content in seawater is three orders of magnitude higher than that of terrestrial water (Koepnick et al., 1985), and a small proportion (<10%) of seawater addition would severely decrease the Sr isotope composition of lake water. Though the mantle-sourced hydrothermal fluid with an extremely low $^{87}Sr/^{86}Sr$ value (0.7035) may play an alternative role, the possibility has already been ruled out as discussed before. The $^{87}Sr/^{86}Sr$ values of a typical mantle-hydrothermal originated dolomite, *e.g.*, Lucaogou Formation are 0.704618–0.705687, lower than our results. In this view, seawater intrusion is more likely to be the reason for low Sr isotopic values. Evidence supporting seawater intrusion event in the Songliao Basin during Late Cretaceous has been widely reported, especially for Nenjiang Formation, of which the dolomite nodule shared the similar Sr isotope (0.70780±0.0005) (Liu and Wang, 1997) with ours.

By assuming a constant rate of seawater reflux into the Songliao Basin and a rapid mixing with the resident lake water, the $^{87}Sr/^{86}Sr$ ratio of the brine mixture is sensitive to seawater proportion. Then the seawater addition can be quantified as following (Stein et al., 2000):

$$\left(\frac{^{87}Sr}{^{86}Sr}\right)_{lw} = \frac{\left(\frac{^{87}Sr}{^{86}Sr}\right)_{sw} \times Sr_{sw} \times f_{sw} + \left(\frac{^{87}Sr}{^{86}Sr}\right)_{tw} \times Sr_{tw} \times (1 - f_{sw})}{Sr_{sw} \times f_{sw} + Sr_{tw} \times (1 - f_{sw})} \quad (4)$$

where subscript *lw*, *sw* and *tw* denote the mixed lake water, seawater and local terrestrial water, respectively. $(^{87}Sr/^{86}Sr)_{lw}$, $(^{87}Sr/^{86}Sr)_{sw}$ and $(^{87}Sr/^{86}Sr)_{tw}$ are Sr isotopes; Sr_{sw} and Sr_{tw} are Sr concentrations in moles; f_{sw} and $(1\text{-}f_{sw})$ are the fractions of seawater and terrestrial water, respectively. The values of various coefficients in Eq. (4) were obtained as: $(^{87}Sr/^{86}Sr)_{sw}$=0.70742 at 90 Ma from (Mearon et al., 2003); $(^{87}Sr/^{86}Sr)_{tw}$=0.7119 is from modern river (Palmer and Edmond, 1989); Sr_{sw}=0.097 mmol/L is from modern seawater (Koepnick et al., 1985); Sr_{tw}=0.001 mmol/L is from modern river (Livingstone, 1964). As shown in **Fig. 13**, the contribution of seawater was negligible (0.78%) during black shale sedimentation, whereas become intensive (6.7%) at transitional zone, and surged to 16.4%–19.7% within dolomite, possibly indicating a gradually enhanced seawater intrusion event. The outer space of dolomite nodule had went through more influential seawater alternation than core area.

Fig. 13. Dependency of $^{87}Sr/^{86}Sr$ on seawater addition, superimposed with modern river (Palmer et al., 1989), shale and dolomite samples here in this study. Seawater addition shows an increasing trend from core to outer space in dolostone.

494 4.4 Implications on the seawater intrusion in the Songliao Basin

495 Increasing evidence proves that dolomite can generate with microbial mediations, including sulfate
496 reduction (Vasconcelos and McKenzie, 1997), anaerobic methane-consuming (Hinrichs et al., 1999),
497 methanogenic model (Roberts et al., 2004; Sun et al., 2020) and aerobic oxidation (Sánchez-Román et
498 al., 2008). Dolostones in the Qingshankou Formation as thin layers and nodules (**Fig. 14**) take up no
499 more than 5% of the total thickness. They are different from those evaporation-originated massive
500 dolostone bodies with hundreds of meters in thickness and hundreds of kilometers in lateral extent in
501 Paleozoic and Precambrian sedimentary successions (Chang et al., 2020). The Late Cretaceous period
502 has been characterized with notable oceanic anoxic events (OAEs), which were closely linked to the
503 reorganization of ocean circulation patterns, while potentially enhanced by widespread rifting and
504 volcanism (Cao et al., 2016; Jones et al., 2018). However, it is still unclear whether the global marine
505 events have teleconnections to the terrestrial realm through either atmospheric process or seawater
506 intrusion into continental margin basins. Insofar as ridge volume provides a first order control on
507 eustatic sea level, it is plausible that the lacustrine Songliao Basin was episodically flooded in response
508 to global tectonic activity during the Cretaceous Period (Cao et al., 2016). Here, based on the Y/Ho
509 values and Sr isotope compositions of a dolomite nodule, the connection between the dolomitization
510 and seawater interference is established, which provides new petrological evidence supporting seawater
511 intrusion events in the Songliao Basin. These events may have contributed to changes in lake water
512 chemistry and redox condition of bottom lake, and therefore organic carbon burial. The rhythmic
513 occurrence of dolomite may be compared with TOC cycles (Huang et al., 2021), and therefore helpful
514 for unconventional petroleum (e.g., shale oil) exploitation.

515

516 **Fig. 14**. Laminar (a) and nodular (b) dolostones of Qingshankou Formation in outcrop.

517

518 In this view, we propose that the dolostone embedded in the basal black shale of Qingshankou
519 Formation might be attributed to the increasing salinity and varied water redox condition that associated
520 with seawater intrusion (**Fig. 15**). Before seawater intrusion, the Songliao Basin was supposed to be a
521 stagnant pool of anoxic bottom-water with "biogenic meromixis" prompted water column stratification
522 (Boehrer and Schultze, 2008), being conducive to mass sedimentation of TOC-rich black shale (Jones
523 et al., 2018) (**Fig. 15a**). The stagnant bottom water was interrupted by episodic seawater flooding, which
524 swept over the land blocking lake and sea, while bringing mass terrigenous detritus and water with high
525 salinity (*e.g.*, Ca^{2+}, Mg^{2+}, SO_4^{2-}, FeOOH, $Fe_2O_3 \cdot nH_2O$) into the lake as dolomitization reactants. Organic
526 matter was degraded via the activated methanogenesis and sulfate reduction (Berner, 1984; Fredrickson
527 et al., 2000) (which will be confirmed by further measurements on $\delta^{13}C$ and $\delta^{18}O$ values), while giving
528 rise to dolomite precipitation and a possible lacustrine oxygen minimum zone (OMZ) (**Fig. 15b**). As
529 methanogenesis gradually took over sulfate reduction, excessive Fe^{2+} could no longer be captured by
530 limited H_2S products, thereby entered dolomite lattice as ankerite crystals (Fe-dolomite). After seawater
531 intrusion, the subsequent water stratification from dissolved biochemical products might probably
532 inhibit lake overturning and oxygenation of bottom-waters, and resulted in an extremely reducing
533 environment again, which facilitated the sedimentation of black shales (**Fig. 15c**).

534

535 **Fig. 15**. Schematic diagrams of the scenario before (a), during (b) and after (c) seawater intrusion in
536 the Songliao Basin.

537

5. Conclusion

Lacustrine dolostone embedded in black shales bears great scientific significance upon its genesis, of which the geochemical analyses, including elemental and isotopic investigation have been widely conducted. Based on *in-situ* microscopic observation and elemental characterization with high resolution, a lacustrine dolomite nodule from the Qingshankou Formation in the Songliao Basin has been confirmed with a penecontemporaneous origin. After excluding potential terrigenous contamination, the lake water sourced REE+Y patterns of dolomite are featured by middle REE enrichment, low Y/Ho and inconspicuous positive Ce, Eu anomalies. The values of $^{87}Sr/^{86}Sr$ within the dolomite nodule (0.7076–0.7080) are slightly higher than the contemporaneous seawater (0.7074), whereas far negative than the host black shale (0.7100). Compared with other Cenozoic-Mesozoic lacustrine dolomites formed in fresh lake water ($^{87}Sr/^{86}Sr>0.7120$), the low Sr isotopes may be attributed to a mixing of seawater with a percentage of no more than 20%. It is supposed that dolostones from the Qingshankou Formation could be a novel mineralogical indicator supporting episodic seawater intrusion events in the Songliao Basin, which supplemented other paleontological and geochemical evidence.

Acknowledgement

The research is financially supported by Project of Basic Science Center of National Natural Science Foundation of China (72088101), the Strategic Priority Research Program of the Chinese Academy of Sciences (XDA14010101), National Key Research and Development Program of China (2017YFC0603101), National Natural Science Foundation of China (41872125, 42002158), Scientific and Technological Project of RIPED (2021ycq01) and the subject development project of RIPED (yjkt2019-3). We are grateful to Editor Zhu Teng, Associate Editor Song Zezhang, and reviewers for their instructive comments and suggestions that significantly help to clarify this manuscript. Thanks also give to Exploration and Development Research Institute of Daqing Oil Field Company for sample provision.

References

Alibrahim A, Duane MJ, Dittrich M. Dolomite genesis in bioturbated marine zones of an early-middle Miocene coastal mud volcano outcrop (Kuwait). Sci. Rep. 2021; 11(1): 6636-6654. http://doi.org/10.1038/s41598-021-85978-w.

Azmy K, Brand U, Sylvester P et al. Biogenic and abiogenic low-Mg calcite (bLMC and aLMC): Evaluation of seawater-REE composition, water masses and carbonate diagenesis. Chem. Geo. 2011; 280(1-2): 180-190. http://doi.org/10.1016/j.chemgeo.2010.11.007.

Bau M, Möller P. Rare earth element fractionation in metamorphogenic hydrothermal calcite, magnesite and siderite. Mineral. Petrol. 1992; 45(3): 231-246. http://doi.org/10.1007/BF01163114.

Bechtel A, Jia J, Strobl SAI et al. Palaeoenvironmental conditions during deposition of the Upper Cretaceous oil shale sequences in the Songliao Basin (NE China): Implications from geochemical analysis. Org. Geochem. 2012; 46: 76-95. http://doi.org/10.1016/j.orggeochem.2012.02.003.

Berner RA. Sedimentary pyrite formation: An update. Geochim. Cosmochim. Acta. 1984; 48(4): 605-615. http://doi.org/10.1016/0016-7037(84)90089-9.

Boehrer B, Schultze M. Stratification of lakes. Rev. Geophys. 2008; 46(2): 1-27. http://doi.org/10.1029/2006RG000210.

Bolhar R, Kranendonk MV. A non-marine depositional setting for the northern Fortescue Group, Pilbara Craton, inferred from trace element geochemistry of stromatolitic carbonates. Precambrian Res. 2007; 155(34): 229-250. http://doi.org/10.1016/j.precamres.2007.02.002.

583 Bosio G, Malinverno E, Collareta A et al. Strontium Isotope Stratigraphy and the thermophilic fossil
584 fauna from the middle Miocene of the East Pisco Basin (Peru). J. S. Am. Earth Sci. 2020; 97:
585 102399. http://doi.org/https://doi.org/10.1016/j.jsames.2019.102399.
586 Bwire Ojiambo S, Berry Lyons W, Welch KA et al. Strontium isotopes and rare earth elements as
587 tracers of groundwater–lake water interactions, Lake Naivasha, Kenya. Appl. Geochem. 2003;
588 18(11): 1789-1805. http://doi.org/10.1016/s0883-2927(03)00104-5.
589 Cao H, Kaufman AJ, Shan X et al. Sulfur isotope constraints on marine transgression in the lacustrine
590 Upper Cretaceous Songliao Basin, northeastern China. Palaeogeogr. Palaeoclimatol.
591 Palaeoecol. 2016; 451: 152-163. http://doi.org/10.1016/j.palaeo.2016.02.041.
592 Carlo E, Wen XY, Irving M. The Influence of Redox Reactions on the Uptake of Dissolved Ce by
593 Suspended Fe and Mn Oxide Particles. Aquat. Geochem. 1997; 3(4): 357-389.
594 http://doi.org/10.1023/a:1009664626181.
595 Chanda P, Fantle MS. Quantifying the effect of diagenetic recrystallization on the Mg isotopic
596 composition of marine carbonates. Geochim. Cosmochim. Acta. 2017; 204: 219-239.
597 http://doi.org/10.1016/j.gca.2017.01.010.
598 Chang B, Li C, Liu D et al. Massive formation of early diagenetic dolomite in the Ediacaran ocean:
599 Constraints on the "dolomite problem". Proc. Natl. Acad. Sci. U. S. A. 2020; 117(25):
600 201916673. http://doi.org/10.1073/pnas.1916673117.
601 Dia A, Gruau G, Olivié-Lauquet G et al. The distribution of rare earth elements in groundwaters:
602 assessing the role of source-rock composition, redox changes and colloidal particles. Geochim.
603 Cosmochim. Acta. 2000; 64(24): 4131-4151. http://doi.org/10.1016/S0016-7037(00)00494-4.
604 Dulski B. Yttrium and lanthanides in eastern Mediterranean seawater and their fractionation during
605 redox-cycling. Mar. Chem. 1997; 56(1-2): 123-131. http://doi.org/10.1016/S0304-
606 4203(96)00091-6.
607 Fantle MS, Barnes BD, Lau KV. The Role of Diagenesis in Shaping the Geochemistry of the Marine
608 Carbonate Record. Annu. Rev. Earth Planet. Sci. 2020; 48(1): 549-583.
609 http://doi.org/10.1146/annurev-earth-073019-060021.
610 Faure G. Principles of isotope geology. Earth-Sci Rev. 1978; 14(2): 190-191.
611 Feng ZQ, Jia CZ, Xie XN. Tectonostratigraphic units and stratigraphic sequences of the nonmarine
612 Songliao basin. Basin Research. 2010; 22: 79-95. http://doi.org/10.1111/j.1365-
613 2117.2009.00445.x.
614 Fredrickson JK, Kostandarithesk HM, Li SW et al. Reduction of Fe(III),Cr(VI), U(VI), and Tc(VII) by
615 Deinococcus radiodurans R1. Appl. Environ. Microbiol. 2000; 66: 2006-2011.
616 http://doi.org/10.1128/AEM.66.5.2006-2011.2000.
617 Fruth I, Scherreiks R. Hauptdolomit (Norian)—stratigraphy, paleogeography and diagenesis. Sediment.
618 Geol. 1982; 32(3): 195-205. http://doi.org/10.1016/0037-0738(82)90050-1.
619 Gao X, Wang P, Li D et al. Petrologic characteristics and genesis of dolostone from the Campanian of
620 the SK-I Well Core in the Songliao Basin, China. Geosci. Front. 2012; 3(5): 669-680.
621 http://doi.org/10.1016/j.gsf.2011.12.014.
622 Gao X, Wang P, Li Q et al. The precise naming and mineralogical characteristics of ferruginous
623 lacustrine dolomite in Well CCSD -SK. Acta Petrol. Mineral. 2010; 29(2): 213-218.
624 http://doi.org/1000-6524(2010) 02-0213-06.
625 Gao Y, Ibarra DE, Wang C et al. Mid-latitude terrestrial climate of East Asia linked to global climate
626 in the Late Cretaceous. Geology. 2015; 43(4): 287-290. http://doi.org/10.1130/g36427.1.
627 Goldstein SJ, Jacobsen SB. Rare earth elements in river waters. Earth Planet. Sci. Lett. 1988; 89(1): 35-
628 47. http://doi.org/10.1016/0012-821X(88)90031-3.

Gong Q, Li F, Lu C et al. Tracing seawater- and terrestrial-sourced REE signatures in detritally contaminated, diagenetically altered carbonate rocks. Chem. Geo. 2021; 570: 120169. http://doi.org/10.1016/j.chemgeo.2021.120169.

Gregg JM, Bish DL, Kaczmarek SE et al. Mineralogy, nucleation and growth of dolomite in the laboratory and sedimentary environment: A review. Sedimentology. 2015; 62(6): 1749-1769. http://doi.org/10.1111/sed.12202.

Ha Y, Satish-Kumar M, Park K-H et al. Carbon, oxygen and strontium isotope geochemistry of the late Neoproterozoic carbonate platform deposit Hyangsanni Dolomite of the Okcheon metamorphic belt, Korea. Lithos. 2021; 396-397: 106219. http://doi.org/10.1016/j.lithos.2021.106219.

Haley BA, Klinkhammer GP, McManus J. Rare earth elements in pore waters of marine sediments. Geochim. Cosmochim. Acta. 2004; 68(6): 1265-1279. http://doi.org/10.1016/j.gca.2003.09.012.

Hecht L, Freiberger R, Gilg HA et al. Rare earth element and isotope (C, O, Sr) characteristics of hydrothermal carbonates: genetic implications for dolomite-hosted talc mineralization at Göpfersgrün (Fichtelgebirge, Germany). Chem. Geo. 1999; 155(1): 115-130. http://doi.org/https://doi.org/10.1016/S0009-2541(98)00144-2.

Hinrichs KU, Hayes JM, Sylva SP et al. Methane-consuming archaebacteria in marine sediments. Nature. 1999; 398(6730): 802-805.

Hu JF, Peng PA, Liu MY et al. Seawater Incursion Events in a Cretaceous Paleo-lake Revealed by Specific Marine Biological Markers. Sci. Rep. 2015; 5: 9508. http://doi.org/10.1038/srep09508.

Huang H, Gao Y, Ma C et al. Organic carbon burial is paced by a ~173-ka obliquity cycle in the middle to high latitudes. Sci. Adv. 2021; 7(28): 9489-9498. http://doi.org/10.1126/sciadv.abf9489.

Huang SJ, Huang Y, Lan YF et al. A comparative study on strontium isotope composition of dolomites and their coeval seawater in the Late Permian-Early Triassic, NE Sichuan basin. Acta Petrol. Sin. 2011; 27(12): 3831-3842. http://doi.org/10.1016/S1002-0160(11)60127-6.

Huang Y, Yang G, Gu J et al. Marine incursion events in the Late Cretaceous Songliao Basin: Constraints from sulfur geochemistry records. Palaeogeogr. Palaeoclimatol. Palaeoecol. 2013; 385: 152-161. http://doi.org/10.1016/j.palaeo.2013.03.017.

Jacobsen SB, Kaufman AJ. The Sr, C and O isotopic evolution of Neoproterozoic seawater. Chem. Geo. 1999; 161(1–3): 37-57. http://doi.org/10.1016/S0009-2541(99)00080-7.

Jiang Y, Tan X, Zhang C et al. Genesis of Dolomite in Middle Permian Maokou Formation in Eastern Sichuan: Constraints from In Situ Geochemistry, Sr-Mg Isotopes, and Fluid Inclusions. Geofluids. 2021; 2021: 6611140. http://doi.org/10.1155/2021/6611140.

Jiao X. Feature and Forming Mechanism of Magmatic-hydrothermal Exhalative Sedimentary Rocks in Permian Lucaogou Formation, Xinjiang, Northwest University. 2017.

Johannesson KH, Lyons WB, Yelkin MA et al. Geochemistry of the rare-earth elements in hypersaline and dilute acidic natural terrestrial waters: Complexation behavior and middle rare-earth element enrichments. Chem. Geo. 1996; 133(1-4): 125-144. http://doi.org/10.1016/S0009-2541(96)00072-1.

Jones MM, Ibarra DE, Gao Y et al. Evaluating Late Cretaceous OAEs and the influence of marine incursions on organic carbon burial in an expansive East Asian paleo-lake. Earth Planet. Sci. Lett. 2018; 484: 41-52. http://doi.org/10.1016/j.epsl.2017.11.046.

Kim T, Kim H, Kim G. Tracing river water versus wastewater sources of trace elements using rare earth elements in the Nakdong River estuarine waters. Mar Pollut Bull. 2020; 160: 111589. http://doi.org/10.1016/j.marpolbul.2020.111589.

Koepnick RB, Burke WH, Denison RE et al. Construction of the seawater 87Sr/86Sr curve for the cenozoic and cretaceous: Supporting data. Chem. Geo. 1985; 58(1): 55-81. http://doi.org/10.1016/0168-9622(85)90027-2.

677 Lawrence MG, Greig A, Collerson KD et al. Rare Earth Element and Yttrium Variability in South East
678 Queensland Waterways. Aquat. Geochem. 2006; 12(1): 39-72. http://doi.org/10.1007/s10498-
679 005-4471-8.
680 Li H, Liu Y, Yang K et al. Hydrothermal mineral assemblages of calcite and dolomite–analcime–pyrite
681 in Permian lacustrine Lucaogou mudstones, eastern Junggar Basin, Northwest China. Mineral.
682 Petrol. 2020; 115(1): 63-85. http://doi.org/10.1007/s00710-020-00726-8.
683 Liu B, Wang H, Fu X et al. Lithofacies and depositional setting of a highly prospective lacustrine shale
684 oil succession from the Upper Cretaceous Qingshankou Formation in the Gulong sag, northern
685 Songliao Basin, northeast China. AAPG Bull. 2019; 103(2): 405-432.
686 http://doi.org/10.1306/08031817416.
687 Liu D, Xu Y, Yu Q et al. Catalytic effect of microbially-derived carboxylic acids on the precipitation
688 of Mg-calcite and disordered dolomite: Implications for sedimentary dolomite formation. J
689 Asian Earth Sci. 2020; 193. http://doi.org/10.1016/j.jseaes.2020.104301.
690 Liu W, Wang P. Genesis and Environmental Significance of the Dolomite Concretions from the
691 Nenjiang Formation in the Songliao Basin, Northeastern China. Sediment. Faci. Palaeogeogr.
692 1997; 17(1): 22-26.
693 Livingstone DA. Chemical Composition of Rivers and Lakes. Data of Geochemistry. Washington:
694 United States Government Printing Office. 1964.
695 McArthur JM, Howarth RJ, Shields GA. Strontium Isotope Stratigraphy. The Geologic Time Scale.
696 Boston: Elsevier. 2012. 127-144
697 McLennan SM. Rare earth elements in sedimentary rocks: influence of provenance and sedimentary
698 processes. Rev. Mineral. Geochem. 1989; 21(1): 169-200.
699 Mearon S, Paytan A, Bralower TJ. Cretaceous strontium isotope stratigraphy using marine barite.
700 Geology. 2003; 31(1): 15-18. http://doi.org/10.1130/0091-7613(2003)0312.0.CO;2.
701 Mountjoy EW, Qing H, McNutt RH. Strontium isotopic composition of Devonian dolomites, Western
702 Canada Sedimentary Basin: significance of sources of dolomitizing fluids. Appl. Geochem.
703 1992; 7(1): 59-75. http://doi.org/10.1016/0883-2927(92)90015-U.
704 Nothdurft LD, Webb GE, Kamber BS. Rare earth element geochemistry of Late Devonian reefal
705 carbonates, Canning Basin, Western Australia: confirmation of a seawater REE proxy in
706 ancient limestones. Geochim. Cosmochim. Acta. 2004; 68: 263-283.
707 http://doi.org/10.1016/S0016-7037(03)00422-8.
708 O'Connell B, Wallace MW, Hood AV et al. Iron-rich carbonate tidal deposits, Angepena Formation,
709 South Australia: A redox-stratified Cryogenian basin. Precambrian Res. 2020; 342: 105668.
710 http://doi.org/10.1016/j.precamres.2020.105668.
711 Palmer MR, Edmond JM. The strontium isotope budget of the modern ocean. Earth Planet. Sci. Lett.
712 1989; 92(1): 11-26. http://doi.org/10.1016/0012-821X(89)90017-4.
713 Palmer MR, Elderfield H. Sr isotope composition of sea water over the past 75 Myr. Nature. 1985;
714 314(6011): 526-528. http://doi.org/10.1038/314526a0.
715 Patino LC, Velbel MA, Price JR et al. Trace element mobility during spheroidal weathering of basalts
716 and andesites in Hawaii and Guatemala. Chem. Geo. 2003; 202(3-4): 343-364.
717 http://doi.org/10.1016/j.chemgeo.2003.01.002.
718 Paton C, Hellstrom J, Paul B et al. Iolite: Freeware for the visualisation and processing of mass
719 spectrometric data. J. Anal. At. Spectrom. 2011; 26(12): 2508-2518.
720 http://doi.org/10.1039/C1JA10172B.
721 Planavsky N, Bekker A, Rouxel OJ et al. Rare Earth Element and yttrium compositions of Archean and
722 Paleoproterozoic Fe formations revisited: New perspectives on the significance and
723 mechanisms of deposition. Geochim. Cosmochim. Acta. 2010; 74(22): 6387-6405.
724 http://doi.org/10.1016/j.gca.2010.07.021.

Pourret O, Gruau Gr, Dia A et al. Controls on the distribution of rare earth elements in shallow groundwater. Aquat. Geochem. 2010; 16(1): 31-59. http://doi.org/10.1016/j.watres.2004.04.056.

Rieger P, Magnall JM, Gleeson SA et al. Differentiating between hydrothermal and diagenetic carbonate using rare earth element and yttrium (REE+Y) geochemistry: a case study from the Paleoproterozoic George Fisher massive sulfide Zn deposit, Mount Isa, Australia. Miner. Deposita. 2021; 57: 187–206. http://doi.org/10.1007/s00126-021-01056-1.

Roberts JA, Bennett PC, González LA et al. Microbial precipitation of dolomite in methanogenic groundwater. Geology. 2004; 32(4): 277-280. http://doi.org/10.1130/G20246.2.

Sánchez-Román M, Vasconcelos C, Schmid T et al. Aerobic microbial dolomite at the nanometer scale: Implications for the geologic record. Geology. 2008; 36(11): 879-882. http://doi.org/10.1130/G25013A.1.

Sasmaz A, Zuddas P, Cangemi M et al. Zirconium and hafnium fractionation and distribution of Rare Earth Elements in neutral–alkaline waters: Case study of Lake Van hydrothermal system, Turkey. J. Geochem. Explor. 2021; 226: 106784. http://doi.org/10.1016/j.gexplo.2021.106784.

Shields GA, Webb GE. Has the REE composition of seawater changed over geological time? Chem. Geo. 2004; 204(1-2): 103-107. http://doi.org/10.1016/j.chemgeo.2003.09.010.

Skinner LC, Sadekov A, Brandon M et al. Rare Earth Elements in early-diagenetic foraminifer 'coatings': Pore-water controls and potential palaeoceanographic applications. Geochim. Cosmochim. Acta. 2019; 245: 118-132. http://doi.org/10.1016/j.gca.2018.10.027.

Smrzka D, Zwicker J, Bach W et al. The behavior of trace elements in seawater, sedimentary pore water, and their incorporation into carbonate minerals: a review. Facies. 2019; 65(4): 1-47. http://doi.org/10.1007/s10347-019-0581-4.

Snidvongs AA. The estuarine geochemistry of rare earth elements and indium in the Chao Phraya River,Thailand. Geochim. Cosmochim. Acta. 2000; 64(23): 3983-3994. http://doi.org/10.1016/S0016-7037(00)00473-7.

Stein M, Starinsky A, Agnon A et al. The impact of brine-rock interaction during marine evaporite formation on the isotopic Sr record in the oceans: evidence from Mt. Sedom, Israel. Geochim. Cosmochim. Acta. 2000; 64(12): 2036-2053. http://doi.org/10.1016/S0016-7037(00)00370-7.

Sun F, Hu W, Wang X et al. Methanogen microfossils and methanogenesis in Permian lake deposits. Geology. 2020; 49(1): 13-18. http://doi.org/10.1130/g47857.1.

Taylor SR, McLennan SM. The continental crust: its composition and evolution: An Examination of the Geochemical Record Preserved in Sedimentary Rocks. Oxford: Blackwell Scientific. 1985.

Tostevin R, Shields GA, Tarbuck GM et al. Effective use of cerium anomalies as a redox proxy in carbonate-dominated marine settings. Chem. Geo. 2016; 438: 146-162. http://doi.org/10.1016/j.chemgeo.2016.06.027.

Vasconcelos C, McKenzie JA. Microbial mediation of modern dolomite precipitation and diagenesis under anoxic conditions (Lagoa Vermelha, Rio de Janeiro, Brazil). J. Sediment. Res. 1997; 67(3): 378-390. http://doi.org/10.1306/D4268577-2B26-11D7-8648000102C1865D.

Wang C, Scott RW, Wan X et al. Late Cretaceous climate changes recorded in Eastern Asian lacustrine deposits and North American Epieric sea strata. Earth-Sci Rev. 2013; 126: 275-299. http://doi.org/10.1016/j.earscirev.2013.08.016.

Wang G, Cheng R, Wang P et al. The Forming Mechanism of Dolostone of Nengjiang Formation in Songliao Basin——Example from CCSD-SK II. Acta Geol. Sin-Engl. 2008; 82(1): 48-54.

Wang H, Ye Y, Deng Y et al. Multi-Element Imaging of a 1.4 Ga Authigenic Siderite Crystal. Minerals. 2021; 11: 1395. http://doi.org/10.3390/min11121395.

Wang T, Ramezani J, Wang C et al. High-precision U–Pb geochronologic constraints on the Late Cretaceous terrestrial cyclostratigraphy and geomagnetic polarity from the Songliao Basin,

Northeast China. Earth Planet. Sci. Lett. 2016; 446: 37-44. http://doi.org/10.1016/j.epsl.2016.04.007.

Wen H, Zheng R, Qing H et al. Characteristics of Strontium Isotopic Geochemistry of Sublacustrine Hydrothermal Sedimentary Rock of Xiagou Formation in Qingxi Sag, Jiuquan Basin. Acta Sedimentalogica Sinica. 2009; 27(4): 642-649. http://doi.org/10.1016/S1874-8651(10)60080-4.

Wu H, Zhang S, Hinnov LA et al. Cyclostratigraphy and orbital tuning of the terrestrial upper Santonian–Lower Danian in Songliao Basin, northeastern China. Earth Planet. Sci. Lett. 2014; 407: 82-95. http://doi.org/10.1016/j.epsl.2014.09.038.

Wu H, Zhang S, Jiang G et al. The floating astronomical time scale for the terrestrial Late Cretaceous Qingshankou Formation from the Songliao Basin of Northeast China and its d and paleoclimate implications. Earth Planet. Sci. Lett. 2009; 278(3-4): 308-323. http://doi.org/10.1016/j.epsl.2008.12.016.

Xi D, Cao W, Huang Q et al. Late Cretaceous marine fossils and seawater incursion events in the Songliao Basin, NE China. Cretac. Res. 2016; 62: 172-182. http://doi.org/10.1016/j.cretres.2015.10.025.

Xi D, Wan X, Feng Z et al. Discovery of Late Cretaceous foraminifera in the Songliao Basin: Evidence from SK-1 and implications for identifying seawater incursions. Chin. Sci. Bull. 2011; 56(3): 253-256. http://doi.org/10.1007/s11434-010-4269-y.

Xu F, You X, Li Q et al. Can Primary Ferroan Dolomite and Ankerite Be Precipitated? Its Implications for Formation of Submarine Methane-Derived Authigenic Carbonate (MDAC) Chimney. Minerals. 2019; 9(7). http://doi.org/10.3390/min9070413.

Yang Y. The relationship between geochemistry of dolostone and paleoclimate, transgression: Taking Shahejie Formation in the Qikou depression for example, Jilin University. 2014.

Yang Z, Whitaker FF, Liu R et al. A New Model for Formation of Lacustrine Primary Dolomite by Subaqueous Hydrothermal Venting. Geophys. Res. Lett. 2021; 48(6): 1-11. http://doi.org/10.1029/2020gl091335.

Yang Z, Zhong D, Whitaker F et al. Syn-sedimentary hydrothermal dolomites in a lacustrine rift basin: Petrographic and geochemical evidence from the lower Cretaceous Erlian Basin, Northern China. Sedimentology. 2020; 67(1): 305-329. http://doi.org/10.1111/sed.12644.

Ye Y, Wang H, Wang X et al. In situ rare earth element analysis of a lower Cambrian phosphate nodule by LA-ICP-MS. Geol. Mag. 2020; 158(4): 749-758. http://doi.org/10.1017/s0016756820000850.

Zhang J, Liu G, Cao Z et al. Characteristics and formation mechanism of multi-source mixed sedimentary rocks in a saline lake, a case study of the Permian Lucaogou Formation in the Jimusaer Sag, northwest China. Mar. Petrol. Geol. 2019; 102: 704-724. http://doi.org/10.1016/j.marpetgeo.2019.01.016.

Zhang S, Liu Y, Li H et al. Mantle-originated hydrothermal-sedimentary dolostone in the Middle Permian in eastern Junggar Basin, China. J. Paleontol. 2020; 22(1): 111-128. http://doi.org/10.7605/gdlxb.2020.01.007.

Zhao M. Geochemistry of sedimentary rocks of the late palaeozoic to the earliest Mesozoic in the Lower Yangtze region of South China, University of Science and Technology of China. 2016.

Zhao MY, Zheng YF. Marine carbonate records of terrigenous input into Paleotethyan seawater: Geochemical constraints from Carboniferous limestones. Geochim. Cosmochim. Acta. 2014; 141: 508-531. http://doi.org/10.1016/j.gca.2014.07.001.

Zhao MY, Zheng YF. A geochemical framework for retrieving the linked depositional and diagenetic histories of marine carbonates. Earth Planet. Sci. Lett. 2016; 460: 213-221. http://doi.org/10.1016/j.epsl.2016.11.033.

Zhao Y, Wei W, Li S et al. Rare earth element geochemistry of carbonates as a proxy for deep-time environmental reconstruction. Palaeogeogr. Palaeoclimatol. Palaeoecol. 2021; 574: 110443. http://doi.org/10.1016/j.palaeo.2021.110443.

Zhao Z, Littke R, Zieger L et al. Depositional environment, thermal maturity and shale oil potential of the Cretaceous Qingshankou Formation in the eastern Changling Sag, Songliao Basin, China: An integrated organic and inorganic geochemistry approach. Int. J. Coal Geol. 2020; 232: 103621. http://doi.org/10.1016/j.coal.2020.103621.

Zhou Y, Strandmann P, Zhu M et al. Reconstructing Tonian seawater 87Sr/86Sr using calcite microspar. Geology. 2020; 48(5): 462–467. http://doi.org/10.1130/G46756.1.

Zhu R, Cui J, Luo Z et al. The discussion on the genesis of carbonate concretions in Chang 7 Member of Middle-Upper Triassic Yanchang Formation of Ordos Basin. Acta Geol. Sin-Engl. 2020; 94: 1-13. http://doi.org/10.19762/j.cnki.dizhixuebao.2020000.

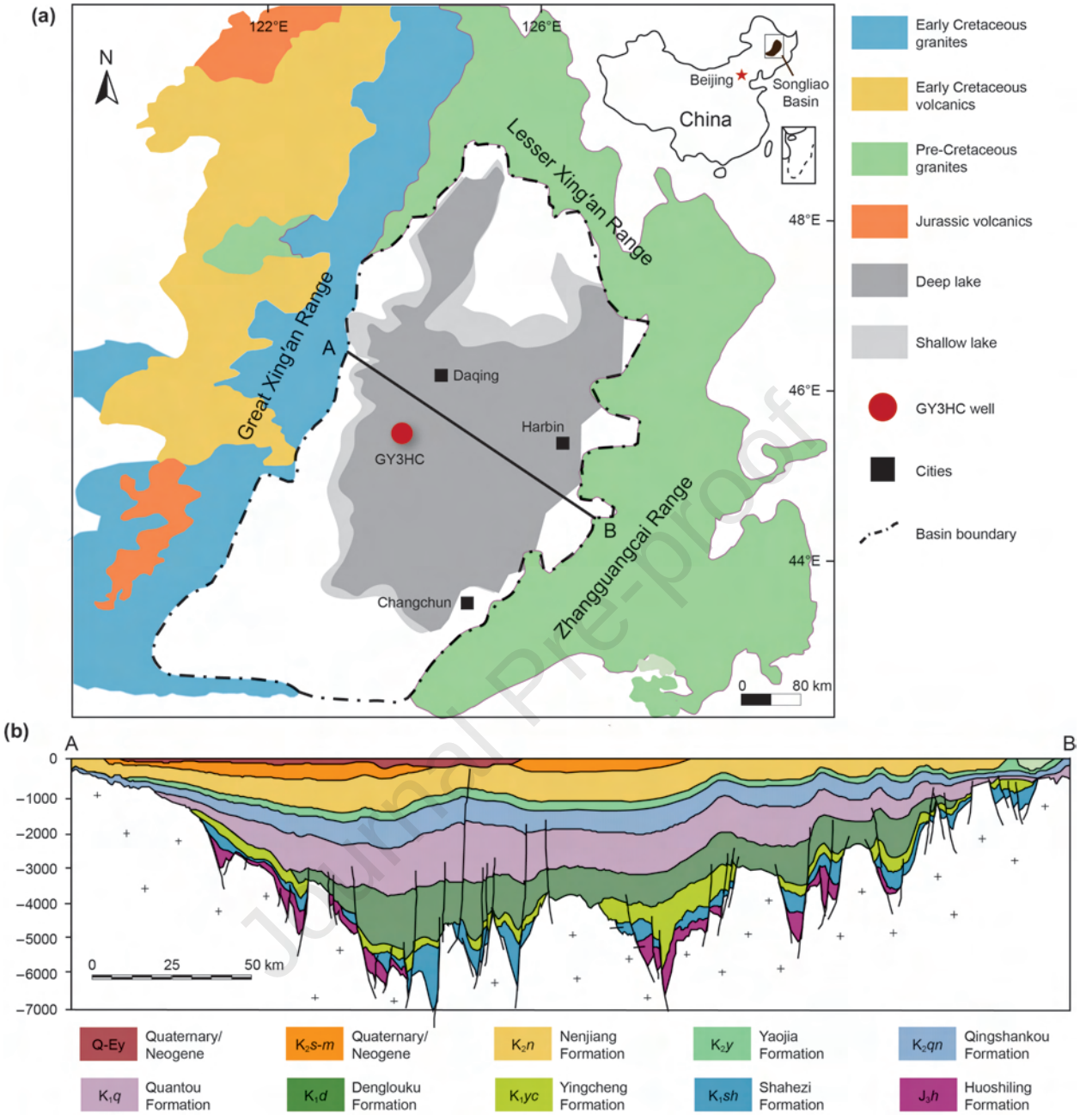

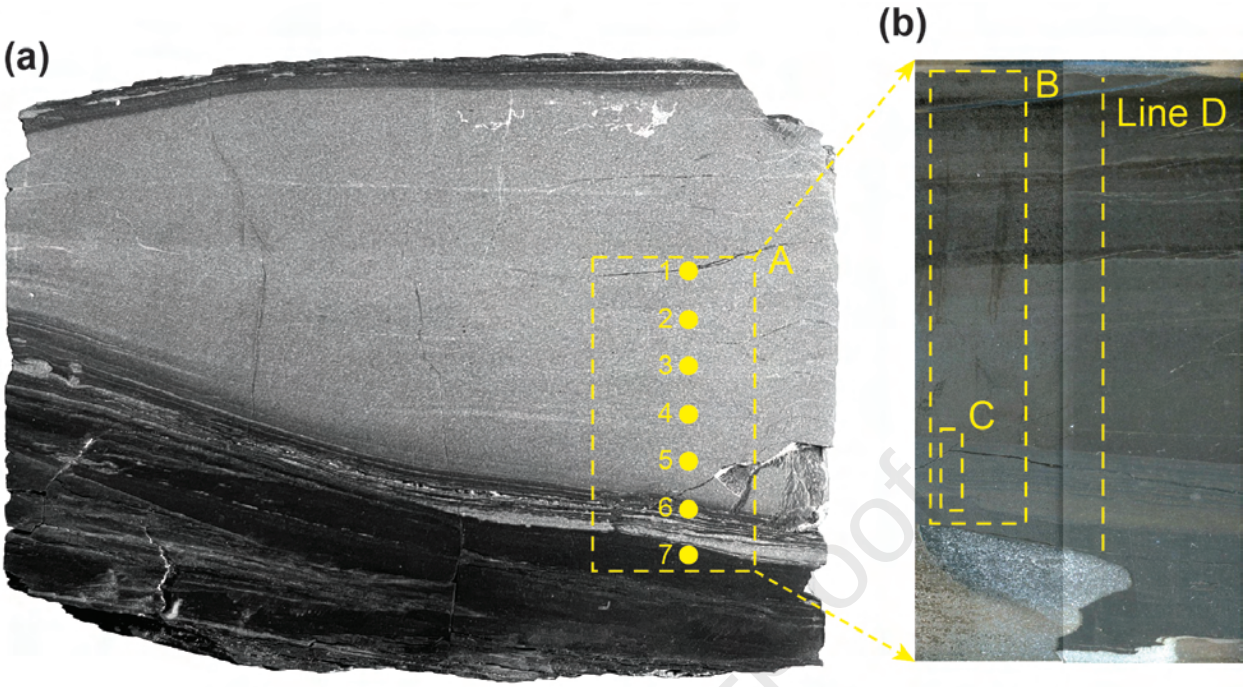

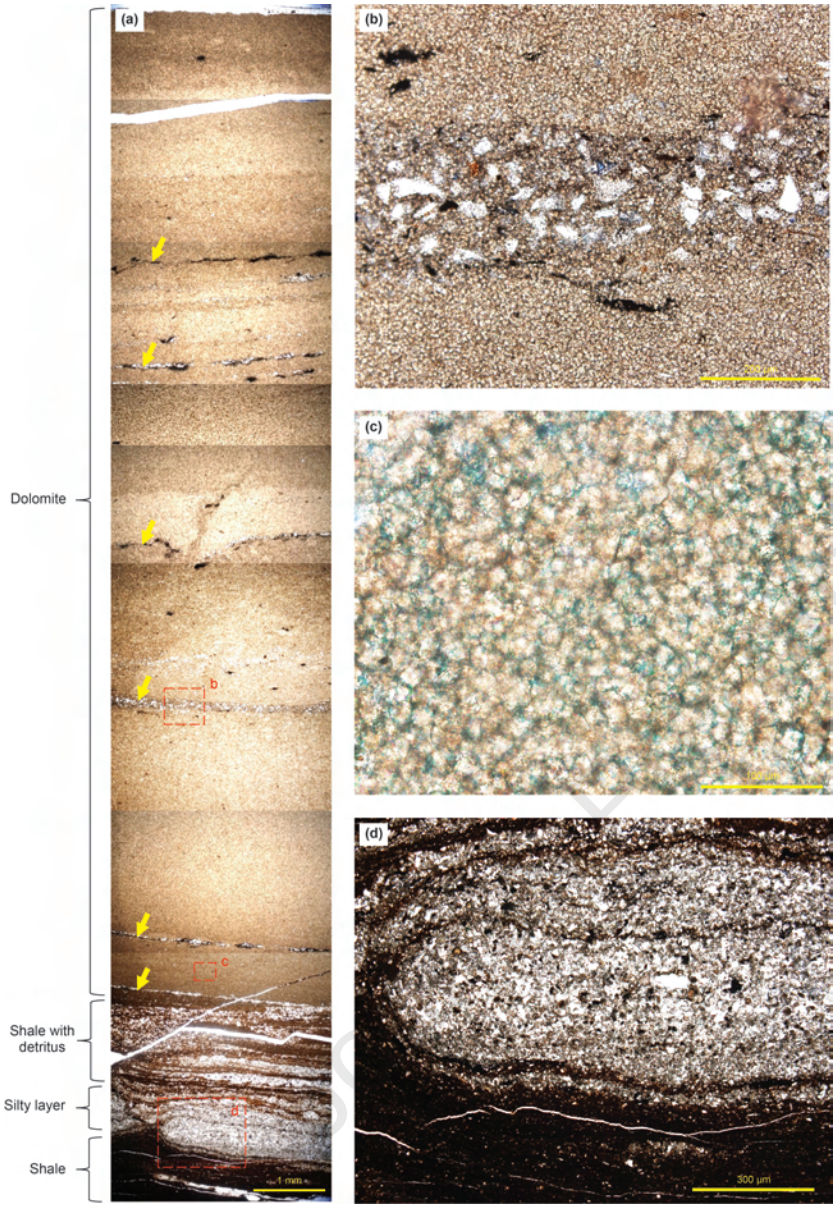
(a)
(b)
(c)
(d)
Dolomite
Shale with detritus
Silty layer
Shale
b
c
d
1 mm
300 µm

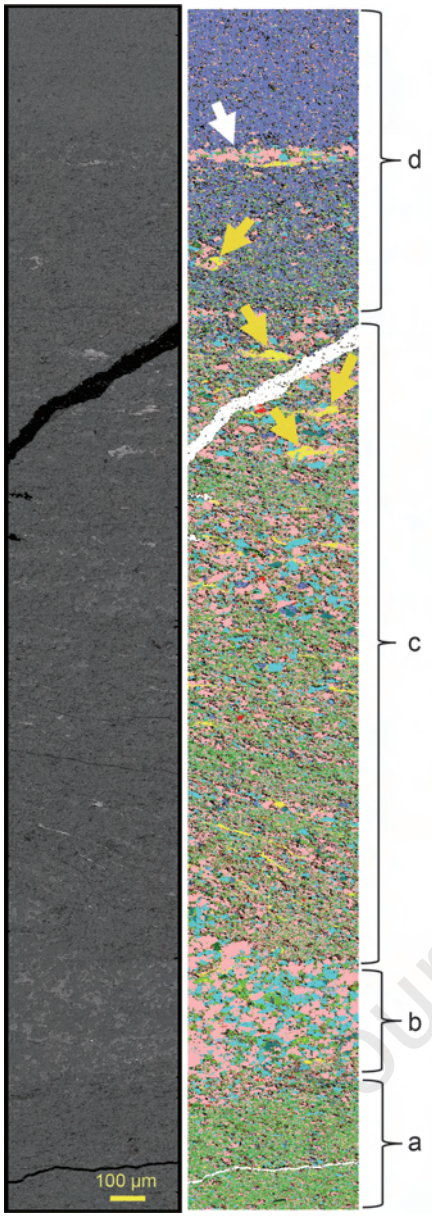

Color	Mineral	Area, %
	Quartz	27.47
	Dolomite	26.15
	Illite	13.65
	Albite	10.39
	Biotite	4.73
	Chlorite	3.42
	Calcite	2.04
	Pyrite	2.04
	K-Feldspar	0.92
	Smectite	0.80
	Muscovite	0.42
	Apatite	0.31
	Rutile	0.30
	Kaolinite	0.14

a: Shale

b: Silty layer

c: Shale with detritus

d: Dolomite